

# Non-Hermitian skin effect in a two-dimensional Lieb photonic crystal

Zhi-Kang Xiong<sup>1</sup>, Tianlei Wen<sup>1</sup>, Y. Liu<sup>1,\*</sup>, Hai Lin<sup>3</sup>, and Bin Zhou<sup>1,2†</sup>

<sup>1</sup> *Department of Physics, School of Physics, Hubei University, Wuhan 430062, P. R. China*

<sup>2</sup> *Wuhan Institute of Quantum Technology, Wuhan 430206, P. R. China*

<sup>3</sup> *College of Physical Science and Technology, Central China Normal University, Wuhan, 430079 P. R. China*

In this contribution paper, we construct a two-dimensional non-Hermitian (NH) photonic crystal (PhC) to prototype its NH skin effect for experimental proposal. Based on the tight-binding model for Lieb lattice with NH coupling, a nontrivial spectral winding number is pinpointed for certain eigenstates, which translates to geometry-dependent skin modes in a PhC slab with tilt boundaries. For ease of implementation, complex refractive indices are employed for the Lieb unit cell of PhC to emulate the NH coupling. Validated by full wave simulation, our work under scores the boundary dependence of the geometric skin effect, and provides a concrete prototype design of NH skin effect easily implemented in classical wave systems by state-of-the-art of topological metamaterial platforms.

## I. INTRODUCTION

Topological band theory, a cornerstone of modern condensed matter physics, has successfully explained a series of novel quantum states, such as topological insulators and topological semimetals, with its core principle being the classification of phases using topological invariants [1–5]. In recent years, this powerful theoretical framework has been successfully extended to NH systems, giving rise to the vibrant frontier of NH topological matter [6–8]. Non-Hermitian systems are ubiquitous in open systems, gain and loss are inherent and controllable physical effects in photonic and acoustic systems [9, 10], while non-equilibrium conditions or finite-lifetime quasiparticles in electronic systems can also be described by NH Hamiltonians [11]. Particularly important is the fact that non-Hermiticity is not always a perturbation but can be ingeniously harnessed to induce new phenomena and applications, such as novel lasers [12, 13], highly sensitive sensors [14–16], and topological energy transport [17, 18].

Existing research on NH topology has largely focused on line-gap topology. In such systems, the energy spectrum possesses a line gap in the complex plane, allowing for the generalization of many concepts from Hermitian topology (e.g., Chern numbers). Within this framework, unique NH phenomena like parity-time (PT) symmetry breaking and exceptional points (EPs) have been extensively studied [6, 8]. EPs are degeneracies unique to NH systems where eigenvalues and eigenvectors coalesce simultaneously, leading to a range of remarkable physical effects, such as sensing enhanced at EPs [14, 19]. However, NH systems also encompass a more fundamental class of topology absent in Hermitian systems, i.e., point-gap topology [8, 20]. Its criterion is whether the system's energy spectrum forms a non-trivial winding around a reference point in the complex energy plane. The most striking macroscopic manifestation of point-gap topol-

ogy is the non-Hermitian skin effect (NHSE) [7, 21–24]. This effect refers to the phenomenon where, under open boundary conditions, the bulk wave functions of the system cease to be extended throughout the space but instead become exponentially localized near the boundaries. This is fundamentally different from the protected boundary states in traditional topological insulators, as the NHSE implies that almost all bulk states become skin modes localized at the boundary. This directional accumulation of bulk waves opens new avenues for applications like directional transport and energy harvesting.

Although the NHSE in one-dimensional systems has been widely reported and deeply understood, its manifestation in higher dimensions is more complex and richer [25–27]. A key theoretical advancement is the recognition that higher-dimensional NHSE exhibits significant geometry-dependence or anisotropy [27, 28]. Its existence strongly depends on the orientation of the system's boundaries. From a topological perspective, if the complex energy bands along a specific direction in the Brillouin zone enclose a non-zero area (i.e., possess a non-zero spectral winding), the skin effect will emerge at the boundaries perpendicular to that direction. This suggests the potential to actively control wave localization by carefully designing the lattice boundaries, enabling unprecedented manipulation of light or sound. Currently, while theoretical research on two-dimensional NH topology has made preliminary progress, systematic studies that tightly integrate point-gap topology, anisotropic NHSE, with specific classical wave (e.g., photonic) lattice models are still relatively scarce. In particular, how non-Hermiticity influences point-gap topology in canonical models like the Lieb lattice, which possesses unique band structures (including flat bands) [29, 30], and how to realize and observe orientation-sensitive NHSE, remain pressing questions to be explored. The Lieb lattice is an important model in PhCs and optical lattice experiments, whose flat band provides an ideal platform for enhancing light-matter interactions and studying localized states. Based on this, this work provides a systematic investigation of point-gap topology and the geometry-dependent NHSE in a two-dimensional NH Lieb lattice.

\* Corresponding author: yangjie@hubu.edu.cn

† Corresponding author: binzhou@hubu.edu.cn

We introduce NH hopping and establish a direct link between the topological spectral winding in the Brillouin zone and the emergence of the skin effect. Our key finding is the prediction and confirmation of a strongly anisotropic NHSE, which manifests only for specific tilted boundaries, achieved through calculations of the winding number and direct observation of wavefunction localization in designed ribbons and finite-sized structures. This study underscores the critical role of boundary design in controlling wave localization within NH systems.

## II. THEORETICAL MODEL AND CALCULATION

Here, we study a normal Lieb lattice model, the structure is shown in Fig. 1(a), whose unit cell includes three

$$H(\mathbf{k}) = \begin{bmatrix} 0 & t_2 + (t_1 + i\gamma)e^{ik_x} & 0 \\ t_2 + (t_1 + i\gamma)e^{-ik_x} & 0 & t_y + t_y e^{-ik_y} \\ 0 & t_y + t_y e^{ik_y} & 0 \end{bmatrix}. \quad (1)$$

The eigen-values of Eq. (1) are:

$$E_0(\mathbf{k}) = 0, \quad E_{\pm}(\mathbf{k}) = \pm \sqrt{M + iN}, \quad (2)$$

where

$$\begin{aligned} M &= t_1^2 + t_2^2 - \gamma^2 + 2t_1 t_2 \cos k_x + 2t_y^2(1 + \cos k_y), \\ N &= 2\gamma(t_1 + t_2 \cos k_x). \end{aligned} \quad (3)$$

When  $\gamma = 0$ , the system is Hermitian, the band structure is shown in Fig. 1(b), which shows a typical flat band. When  $\gamma \neq 0$ , the system is NH due to the complex hopping  $t_1 + i\gamma$ , where the  $\gamma$  represents gain (or loss) of such a NH system. For the NH system, the band structures are shown in Figs. 1(c) and (d), there exist non-zero imaginary components in their energy spectrum. More importantly, there are EPs( $k_x, k_y$ ), where two non-zero eigenvalues and their corresponding eigenstates simultaneously become degenerate [cf. Fig. A1 in Append. A]. According to Eq. (2), the precise parameter conditions for the existence of EPs can be derived,

$$k_x = \pm \arccos\left(-\frac{t_1}{t_2}\right), k_y = \pm 2 \arccos\left(\sqrt{\frac{\gamma^2 - t_2^2 + t_1^2}{4t_y^2}}\right), \quad (4)$$

In general, the system can host up to four EPs. Since we choose the parameters such that  $t_1 = t_2$ ,  $k_x$  becomes degenerate, which results in the system containing only two EPs ( $EP_1$  and  $EP_2$ ), as shown in Figs. 1(c) and (d). These EPs represent topological defects in the NH band structure, typically carrying non-zero topological charges. Here, we provide the method to calculate the

sublattices A, B, and C. In this model, we only consider the nearest neighbor hopping, the intra-cell and inter-cell hopping along the horizontal direction is non-reciprocal, denoted as  $t_2$  and  $t_1 + i\gamma$ , respectively. The hopping along the vertical direction are reciprocal, with both intra-cell and inter-cell hopping denoted as  $t_y$ . Note that all the parameters  $t_{1,2,y}$  and  $\gamma$  are real, the Hamiltonian of such a system can be written as:

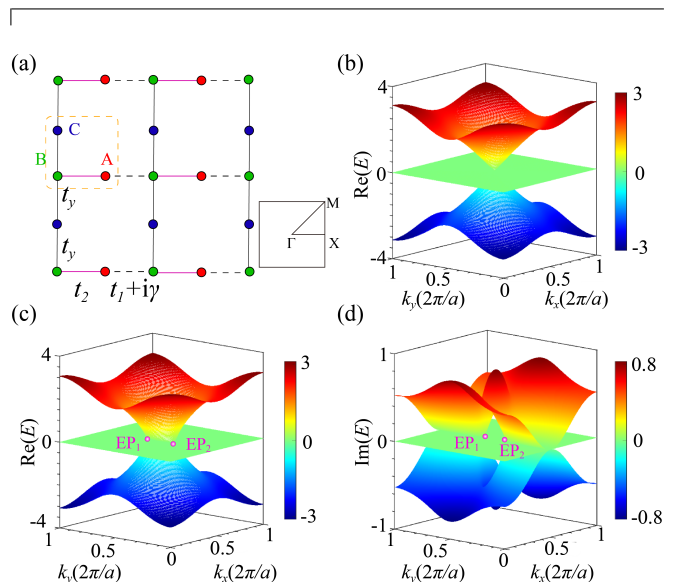


FIG. 1. (a) Schematic for the Lieb lattice, where A, B and C represent three sublattices. The unit cell is marked by an orange dashed line, and the inset represents the first BZ of such a unit cell. (b) Band structure of the Hermitian system with  $\gamma = 0$ , the energy is purely real. (c)-(d) Real and imaginary band structure of the NH system with  $\gamma = 0.8$ . Parameters:  $t_1 = t_2 = 1$ ,  $t_y = 1.2$ .

topological charge of EPs, which can be described by [27, 28]

$$\nu(\mathbf{k}_{\text{EP}}) = \frac{1}{2\pi i} \oint_{\Gamma_{\text{EP}}} d\mathbf{k} \cdot \nabla_{\mathbf{k}} \ln \det[H(\mathbf{k}) - E(\mathbf{k}_{\text{EP}})], \quad (5)$$

where  $\Gamma_{\text{EP}}$  is a closed counterclockwise route enclosing

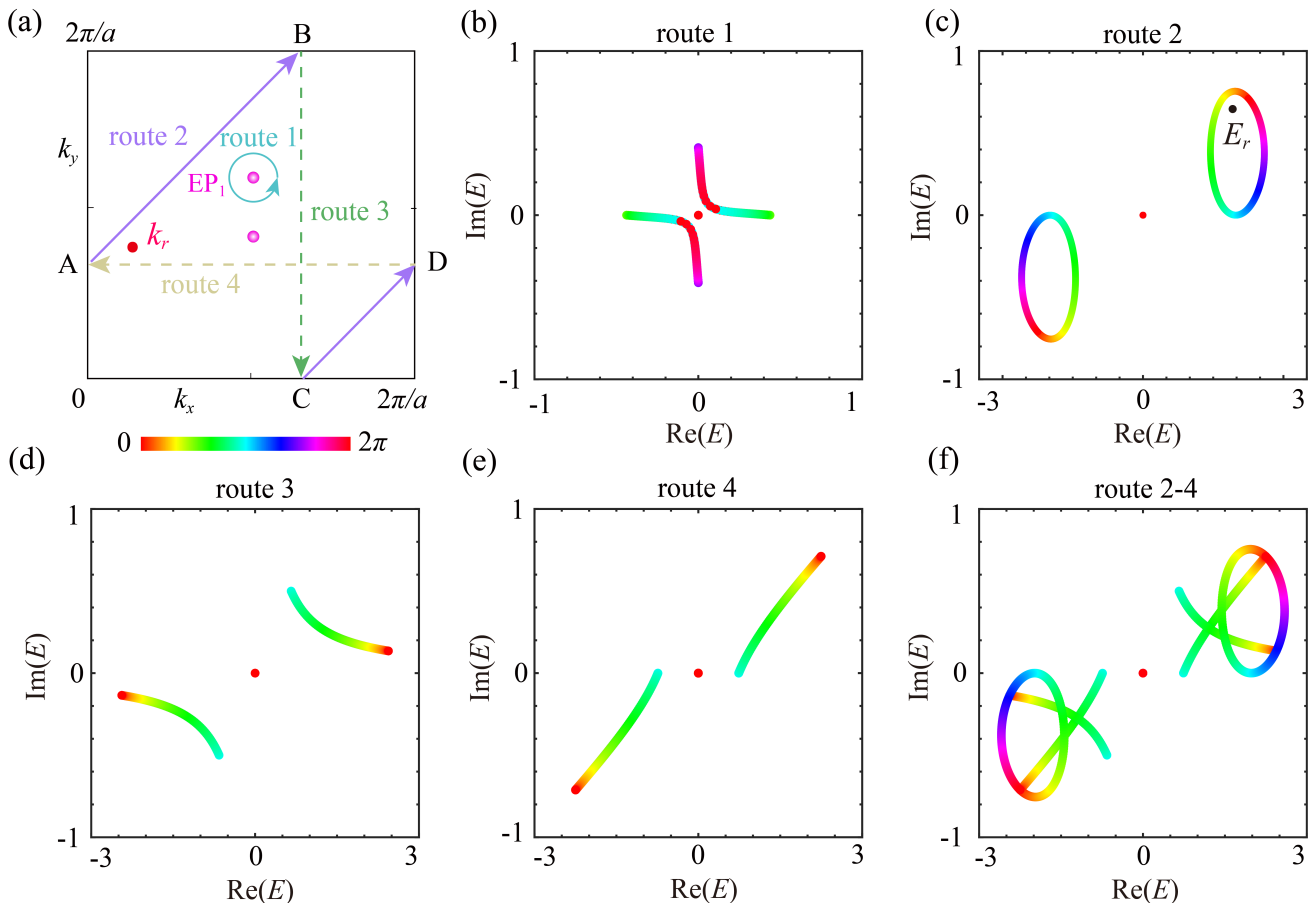


FIG. 2. (a) Different routes in the first BZ, the magenta points represent the EPs, and the red point is the reference point we chose with  $k_r(0.35\pi/a, 0.8\pi/a)$ . (b)-(f) Complex energy spectra of route 1 to route 4. All the parameters are same as those in Fig. 1.

the EP,  $E(\mathbf{k}_{\text{EP}})$  is the energy of EP. This topological charge is actually the spectral winding number of the closed route.

Generally, the EPs profoundly influence the system's bulk-boundary correspondence and the emergence of the NHSE, thereby providing a crucial theoretical foundation for controlling wave propagation and transport properties. However, in our model, the EPs show trivial topological charge, i.e.,  $\nu(\mathbf{k}_{\text{EP}_{1,2}}) = 0$ , the route 1 represent the small closed route  $\Gamma_{\text{EP}}$  we selected, as shown in Fig. 2(a). For trivial topological charge, the complex energy spectrum of such route 1 shows two curves and one point, as shown in Fig. 2(b), corresponding to the three bands of Lieb lattice. Due to the zero energy flat band [cf. Figs. 1(c)-(e)], the energy spectrum will show a point in complex space.

Although the topological charges associated with the EPs are trivial, we find that there exists a reference point  $k_r(0.35\pi/a, 0.8\pi/a)$  in the first BZ which carries a nonzero winding number. This implies that within the BZ, there must exist a closed straight line route  $k_n$  exhibiting a nonzero winding number, which describes the spectral winding around the  $E_r$  on the complex plane,

which is known as the point gap. Further, there will be a geometry dependence on the NHSE emerges at the open boundaries vertical to the  $k_n$  direction [27, 28]. The winding number is defined as

$$\nu(k_r) = \frac{1}{2\pi i} \oint_L d\mathbf{k} \cdot \nabla_{\mathbf{k}} \ln \det[H(\mathbf{k}) - E(r)], \quad (6)$$

where  $L$  is the closed straight line route along the  $k_n$  direction in the first BZ,  $E(r)$  is the energy of reference point  $k_r$ .

Here, we select a closed route  $A \rightarrow B \rightarrow C \rightarrow D \rightarrow A$ , which can be divided into three closed straight line routes 2, 3, and 4, corresponding complex energy spectra are shown in Figs. 2(c)-(e). According to Eq. (6), we find that the  $\nu(k_r) = 0$  for both routes 3 and 4, corresponding complex band do not form the spectral loops, resulting in zero winding number. It means there is no skin effect in the ribbons under rectangle stripe geometry [cf. Fig. A2 in Append. B]. Further, when we open both the boundaries perpendicular to the directions of routes 3 and 4, we obtain a square-shaped super cell. The complex energy spectrum of such square-shaped lattice under open boundary condition (OBC) is shown in Fig. 3(a). For

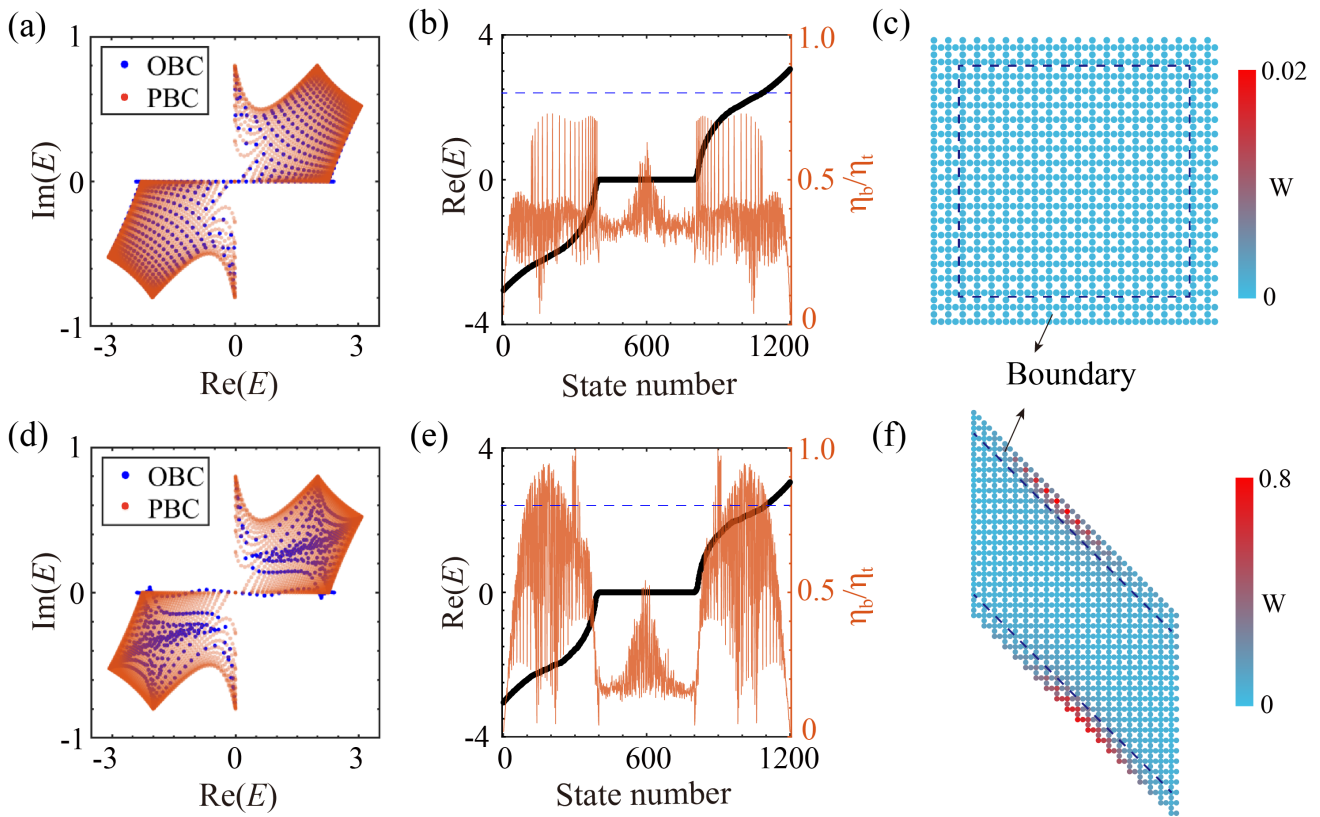


FIG. 3. (a) and (d) Spectral area under square and parallelogram shaped structures under OBC. The red points represent the spectral area under PBC. (b) and (e) The real spectra of two structures, the orange line represents the ratio of the probability density of the wave function at the boundary to that over the entire structures. The blue dashed line represents the degree of localization  $\eta_b/\eta_t = 80\%$  of the probability density at the boundary for each eigenstate. (c) and (f) Spatial distribution of all eigenstates  $W(x)$  distributions of two shaped structures, both consist of  $20 \times 20$  unit cells. The boundary is defined as having a thickness of two unit cells.

comparison, we also plot the complex energy spectrum under periodic boundary condition (PBC). It should be noted that a non-zero area of the complex spectrum under PBC indicates the presence of a geometry-dependent skin effect in the system. In our model, we can see that the spectral area of the square-shaped structure under PBC is same to that under OBC, and there is no skin effect, as shown in Figs. 3(b) and 3(c). Fig. 3(b) shows the real spectrum of the square-shaped structure with  $20 \times 20$  units, where  $\eta_b$  and  $\eta_t$  represent the probability density of the wave function at the boundary and over the entire structure, respectively. To visualize the skin effect, we calculate the spatial distribution of total eigenstates  $W(\mathbf{x})$ , which is defined as [27, 28]

$$W(\mathbf{x}) = \frac{1}{N} \sum_n |\psi_n(\mathbf{x})|^2, \quad (7)$$

where  $\psi_n(\mathbf{x})$  is the  $n$ -th normalized right eigenstate at site  $\mathbf{x}$ , and  $N$  is the number of eigenstates.

On the contrary, for the closed straight line route 2 in Fig. 2(a), the complex energy spectrum of route 2 forms the spectral, resulting in non-zero spectral winding number for the energy of reference point  $E(r)$ , i.e.,

$\nu(k_r) = 1$ , as shown in Fig. 2(c). Non-zero spectral winding number indicates the existence of skin effect at the boundaries perpendicular to the route 2 direction [cf. Fig. A3 in Append. B]. To visualize the skin effect, we design a parallelogram-shaped super cell, including two inclined boundaries perpendicular to the route 2 direction and two vertical boundaries. The spectral area of such parallelogram-shaped lattice under OBC is shown in Fig. 3(d). It exhibits a distribution markedly different from that under PBC, the eigenstates are localized at the two inclined boundaries, which is consistent with our theoretical expectations, manifesting the skin effect, as shown in Figs. 3(e) and 3(f).

### III. NHSE IN LIEB PHC

In Sec. II, we start from a tight-binding model and demonstrate that introducing NH hopping between unit cells of a Lieb lattice can give rise to a geometry-dependent skin effect. To realize this theory, we leverage an optical platform to construct a similar lattice structure. The key lies in how to introduce NH coupling in

PhCs. Here, we introduce the imaginary part of the refractive index to induce wave attenuation during propagation in the medium, thereby creating NH coupling.

For a plane electromagnetic wave in transverse magnetic (TM) mode, its electric field can be expressed as

$$\mathbf{E}(\mathbf{r}, t) = E_0 e^{i\mathbf{k}\cdot\mathbf{r} - i\omega t} \hat{x}, \quad (8)$$

For simplicity, we set  $\mathbf{k} \cdot \mathbf{r} = kz$ , the wave number  $k = n\omega/c$ , where  $n$  is the refractive index of the medium,  $c$  is the speed of the wave within the medium. When the  $n$  is a real number, there is no gain or loss when the electromagnetic wave passes through the media. When the  $n$  is a complex number, i.e.,  $n = n_0 + in_1$ , note that  $n_{0,1} > 0$ . The Eq. (8) can be written as

$$\mathbf{E}(\mathbf{r}, t) = E_0 e^{i(n_0\omega z/c - \omega t)} e^{-n_1\omega z/c} \hat{x}. \quad (9)$$

It means that when an electromagnetic wave propagates through a medium with a complex refractive index, its amplitude undergoes exponential decay, corresponding decay coefficient is  $n_1\omega z/c$ . The energy of electronic field will also be dissipated. To verify this, we design a simple model, as shown in Fig. 4(a). It consists of two circular dielectric rods with radii  $r = 0.13a$  and refractive index  $n_0 = 3.28$ . The two dielectric rods are connected by a rectangular dielectric media serving as a coupler. The background is set to air. Now, we set the left boundary as the input port and the right boundary as the output port. When a plane wave is input from the left boundary and output from the right boundary, the distributions of the reflection (R), transmission (T), and absorption (A) rates of the wave field with respect to variations in the refractive index  $n$  of the rectangular dielectric are shown in Fig. 4(b). Here, we first assume that the imaginary part of the refractive index  $\text{Im}(n) = 0$ , the absorption rate is always zero, which implies that no energy loss occurs. When we fix  $\text{Re}(n) = 1.87$ , and we introduce imaginary refractive index  $\text{Im}(n)$ , as the  $\text{Im}(n)$  gradually increases, the absorption rate also rises, indicating a corresponding increase in energy loss until it eventually stabilizes, as shown in Fig. 4(c). Thus, we can analogize the definition of the medium's refractive index to the hopping in the tight-binding model, the Lieb PhC model is shown in Fig. 4(d).

For such Lieb PhC, the band structures are shown in Figs. 5(a) and 5(b). Here, we calculated five energy bands, among which the first three bands are gapless. Unlike the tight-binding model, there exist no EPs. The first BZ is shown in Fig. 5(c), we select the same three closed path as shown in Fig. 2(a), corresponding complex spectra are shown in Figs. 5(d)-(f).

For simplicity, we consider only the complex spectrum of the first three bands, which are sufficiently representative. For route 1, the complex spectrum forms an open curve with a winding number of zero, as shown in Fig. 5(d). This implies that when open boundaries are applied perpendicular to route 1, the skin effect will not emerge at those boundaries. Particularly, for route

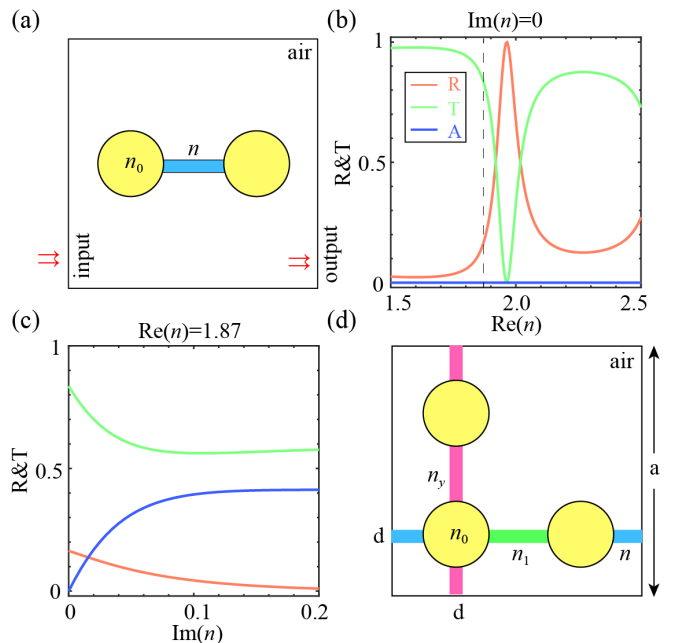


FIG. 4. (a) A model for verifying the impact of refractive index on the energy propagation of electromagnetic waves. (b) The distributions of the reflection (R), transmission (T), and absorption (A) rates of the wave field with respect to variations in the refractive index  $\text{Re}(n)$  and (c)  $\text{Im}(n)$  of the rectangular dielectric media. (d) A PhC model based on the Lieb lattice, which is analogous to the tight-binding model. Parameters:  $n_0 = 3.28$ ,  $n_1 = 1.87$ ,  $n_y = 2$ ,  $n = 1.87 + 0.1i$  and  $d = 0.05a$ .

2, the complex spectrum of the first three bands winds into a closed loop, giving rise nonzero spectral winding number. The complex spectrum of the first band forms a closed loop with  $\nu = -1$ . Interestingly, the complex spectra of the second and third show more complicated winding patterns, such as a triple loop winding, as shown in Fig. 5(e). The band structure exhibits a loop that encircles three distinct regions, each associated with opposite winding directions. The nontrivial spectral winding implies that introducing boundaries perpendicular to route 2 will result in the emergence of the skin effect. Moreover, the bulk band features a self-intersection at the Bloch point [31–33]. In such a scenario, the finite stripe hosts an eigenstate that remains spatially extended and whose eigenfrequency aligns closely with that of the Bloch point. Bloch points are especially significant as they mark an unconventional topological phase transition between two types of edge states, each confined to opposite ends of the stripe. This behavior has led to the interpretation of the Bloch point as indicative of a bipolar skin effect [31]. These isolated delocalized eigenstates represent a hallmark of NH systems and may be exploited in applications such as extended laser modes. Although Bloch points have recently been observed experimentally in topological acoustic systems governed by tight-binding models [26, 28, 34], our work demonstrates their feasibil-

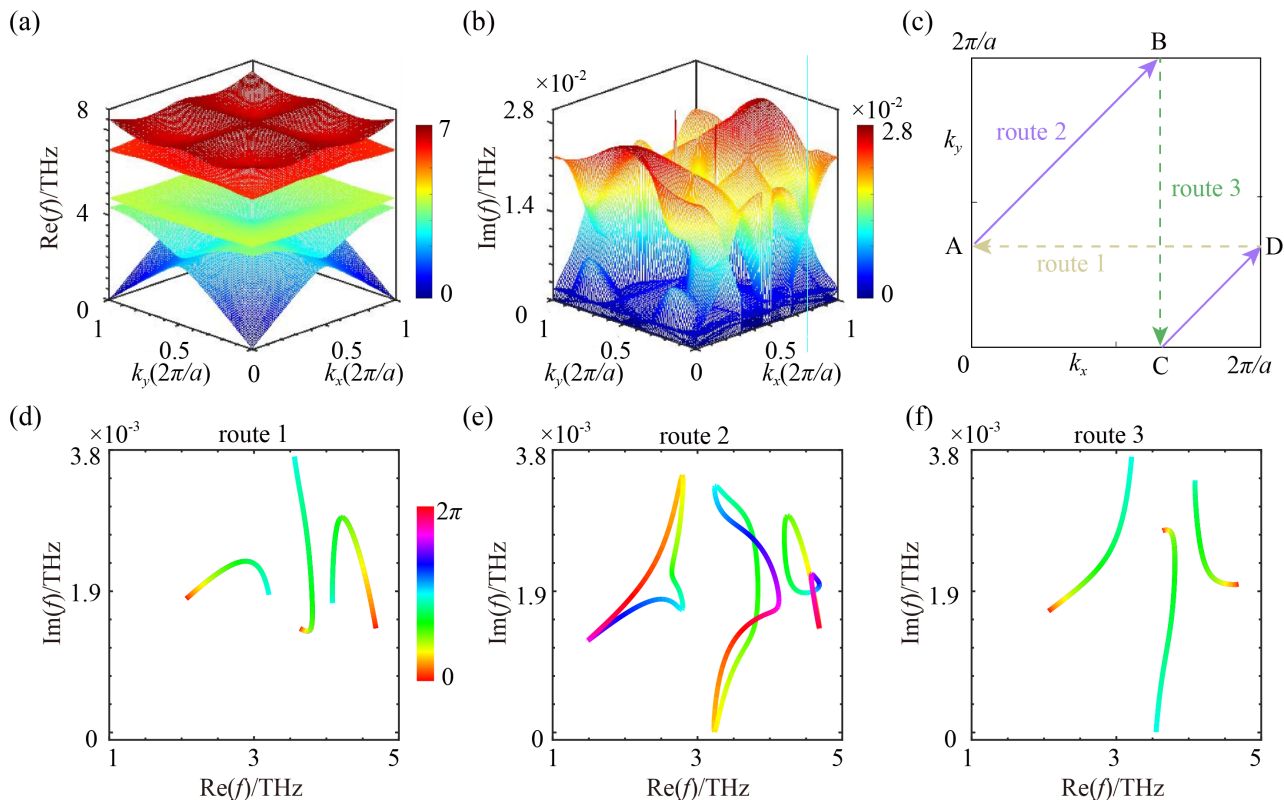


FIG. 5. (a)-(b) The real and imaginary parts of the band structures for the Lieb PhC shown in Fig. 4(d). (c) The first BZ of the Lieb PhC, and we select three closed straight line routes, corresponding to the complex spectra of the three bands are shown in (d)-(f).

ity in reciprocal PhC structures as well. As for route 3, the complex spectrum still forms an open curve with trivial winding, as shown in Fig. 5(f), so there is no skin effect emerge at the boundaries which are perpendicular to route 3 directions.

To verify the PhC skin effect, we have designed two supercells with different open boundaries, as shown in Fig. 6(a) and 6(e). Both structures are composed of  $20 \times 20$  unit cells. For the unit cell structure we designed, the complex energy spectrum under PBCs exhibits a non-zero spectral area [cf. Fig. 6(b)], indicating the presence of the skin effect. For the square-shaped supercell, the complex energy spectrum under OBCs is almost identical to that under PBCs, as shown in Fig. 6(b), and there is no skin effect. Figure 6(c) shows the real spectrum corresponding to the square supercell. Here, we calculated 1200 eigenfrequencies and computed the eigen-electric field distribution for each eigenfrequency, where  $\eta'_b$  represents the electric field energy at the boundary, and  $\eta'_t$  represents the electric field energy of the entire supercell. The ratio of the two indicates the degree of localization of an individual eigen-electric field at the boundary. Here, we also take a thickness of 2 unit cells as the boundary. It should be noted that in the square-shaped supercell, there exist states with a ratio  $\eta'_b/\eta'_t > 80\%$ . Although their eigen-electric fields are localized at the boundary,

as shown in Fig. 6(d), these states are not regarded as skin modes but rather as localized states, because the number of these states does not obey the volume law [cf. Fig. A4(c) in Append. C]. For the parallelogram-shaped structure, its complex energy spectrum under OBCs is clearly different from that under PBCs, indicating that the conventional bulk-boundary correspondence breaks down, as shown in Fig. 6(f). The corresponding real energy spectrum of the parallelogram structure is shown in Fig. 6(g). Here, we also calculated the degree of localization  $\eta'_b/\eta'_t$  of the electric field energy at the boundary for each eigenstate, with the boundary defined as having a thickness of 2 unit cells. There are 33 states that satisfy the condition  $\eta'_b/\eta'_t \geq 80\%$  and are considered as skin modes, which obey the volume law [cf. Fig. A4(c) in Append. C]. We selected the skin mode as shown in Fig. 6(h), and the results show that the electric field energy is localized at the inclined boundary, while there is almost no electric field distribution at the vertical boundary. This is consistent with our previous analysis of the complex energy spectrum.

In addition, we plot the spatial distribution of all eigenstates  $W(x)$  distributions of two shaped structures [cf. Figs. A4(a) and A4(b) in Append. C]. It should be noted that we calculated 1200 states, among which only 33 are skin modes. Therefore, the skin effect is scarcely visible

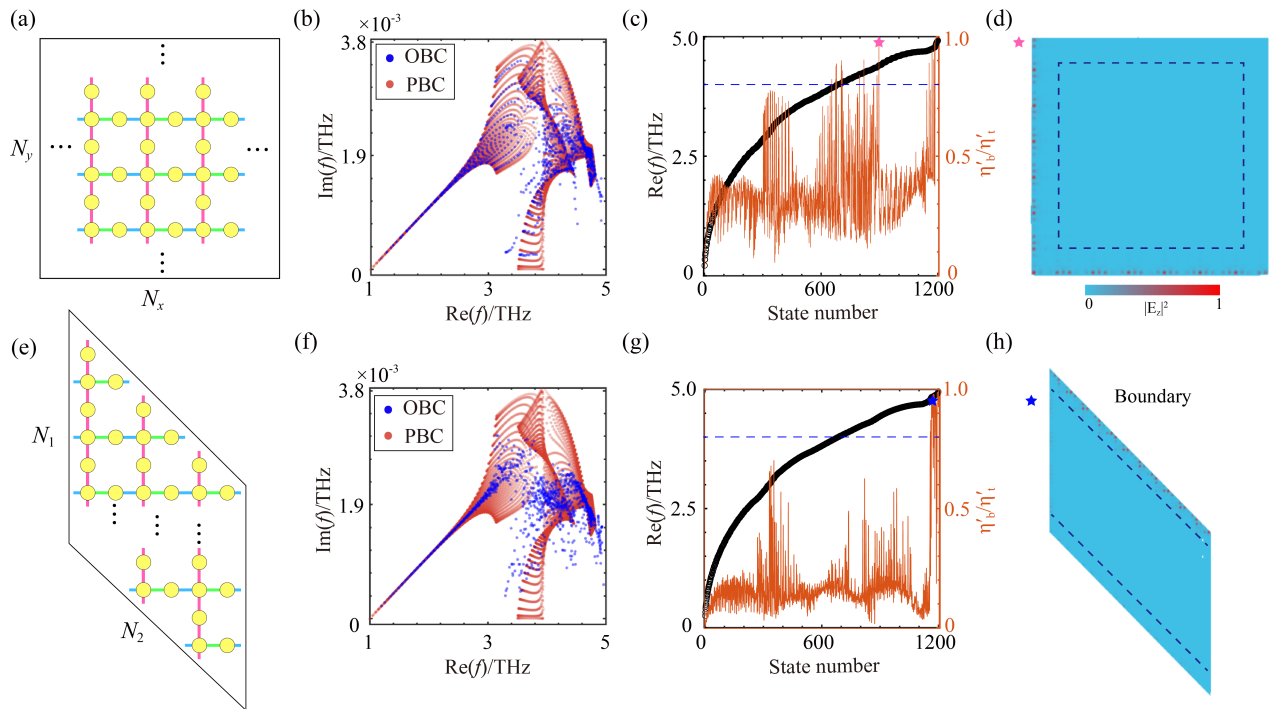


FIG. 6. (a) and (e) Two types of super cell with different open boundaries. (b) and (f) PBC and OBC complex spectra of two supercells. (c) and (g) The OBC spectra of two types of super cell, where  $\eta'_b$  and  $\eta'_t$  represent the electric field energy density at the boundary and of the entire supercell, respectively. The corresponding state numbers are 886 and 1188. (d) and (h) The field distributions of states 1188 and 1170, marked by magenta and blue pentagram, respectively. The number of unit cells  $N_i = 20$ , and the boundary is defined as having a thickness of two unit cells.

in  $W(x)$ .

#### IV. CONCLUSION

In summary, we demonstrate a geometry-dependent NHSE in a two-dimensional Lieb PhC. By introducing NH coupling via complex refractive indices, we realized a photonic analogue of NH hopping. Through spectral winding number analysis, we predicted that the skin effect emerges when boundaries are oriented along specific directions (e.g.,  $y = -x$ ) with nontrivial point-gap topology. In fact, the skin effect also emerges when boundaries are oriented along  $y = x$  direction. Full-wave simulations on parallelogram structures confirmed this behavior: eigenstates localize at inclined boundaries, and the number of skin modes obey the volume law, distinguishing them from ordinary localized states. In contrast, square structures exhibit no skin effect. Our work provides a practical photonic platform for exploring NH topology and geometry-dependent wave localization, with potential applications in directional energy harvesting and sensing.

#### Appendix A: Examination of EPs

In this Append., we selected a series of closed routes in the first Brillouin zone (BZ) to verify our calculation of EPs, and the corresponding energy band diagrams for each contour are plotted, as shown in Fig. A1. For route 1, we select high-symmetry points ( $\Gamma$ , X, and M) in k-space to form a closed loop, where the segment from X to M passes through  $EP_2$ . The corresponding real and imaginary parts of the energy bands will exhibit degeneracy at  $EP_2$ , as shown in Fig. A1(b). The inset shows the eigenstates corresponding to the three degenerate eigenvalues. It can be observed that at the EP, the eigenstates are also degenerate. For route 2, we fix  $k_y = \pi/a$  and define  $k_x$  from 0 to  $2\pi/a$ , this route will pass through high-symmetry point M, and the real part of energy bands exhibit degeneracy, while the imaginary part of energy bands exhibit not, as shown in Fig. A1(c), so the point M is not an EP. For routes 3 and 4, they pass through one EP and two EPs respectively, corresponding the energy bands exhibiting one and two degeneracy points, as shown in Figs. A1(d)-(e). As for route 5, it does not pass through any high-symmetry points or EPs, and its energy bands exhibit no degeneracy, as shown in Fig. A1(f).

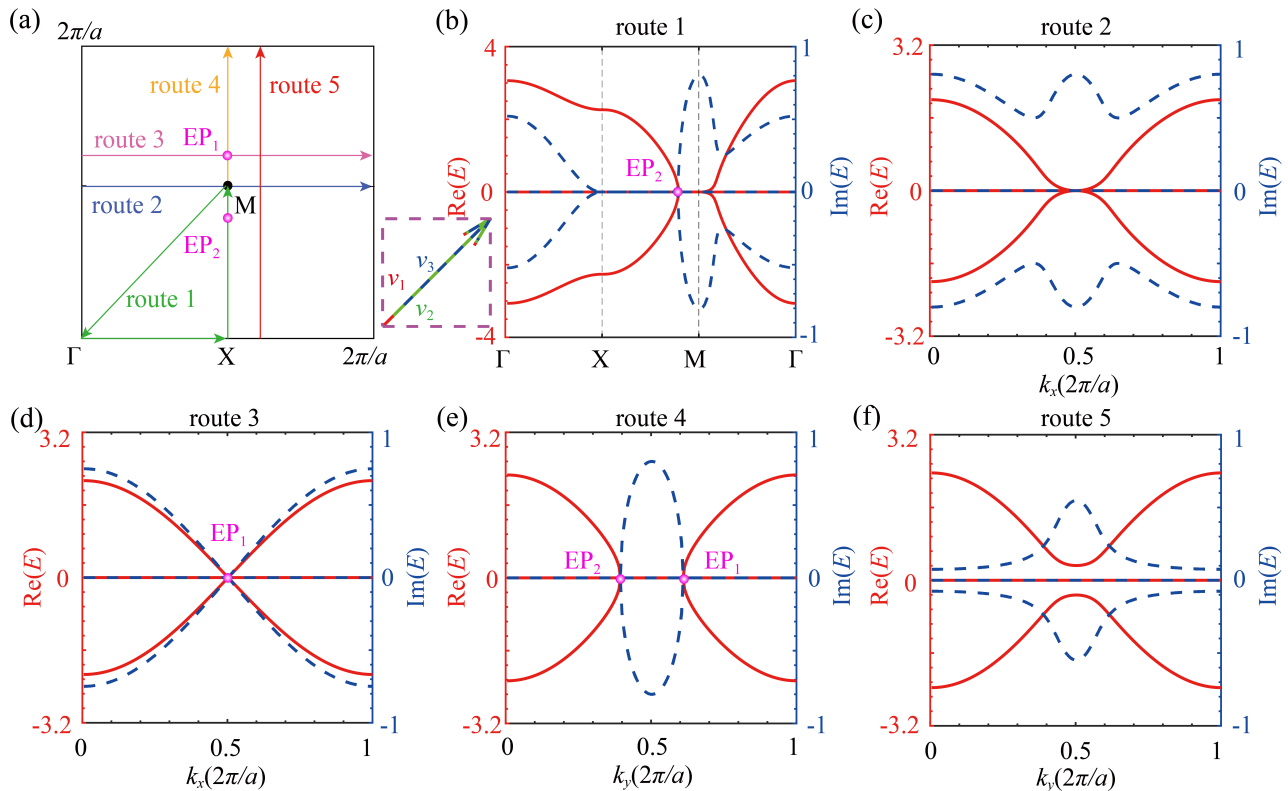


FIG. A1. (a) Different routes in the first Brillouin zone (BZ), the magenta points represent the EPs ( $EP_1$  and  $EP_2$ ). (b)-(f) The real and imaginary band structures of different routes in (a). All the parameters are same as those in Fig. ??.

### Appendix B: NHSE in the 1D ribbons

In this Append., we investigate the ribbons under different shaped structures to verify the existence of skin effect in 1D ribbon. Specifically, we consider a rectangle and a parallelogram-shaped ribbons.

Firstly, for the ribbons under rectangle-shaped, one model is designed with OBCs along the  $x$  direction and PBCs in the  $y$  direction, as shown in Fig. A2(a), where  $N_y = 16$  is the number of unit cell. The projected band of such super cell are shown in Figs. A2(b) and (c), which show zero energy flat bands. Here, we present the spatial distribution of eigenstates corresponding to two points, as shown in Fig. A2(d). Additionally, we judge an eigenstate  $\psi(\mathbf{x})$  as a skin mode when it satisfies

$$\sum_{x \in \mathcal{B}} |\psi(\mathbf{x})|^2 \geq 80\%, \quad (\text{B1})$$

where  $\mathcal{B}$  represents the boundary region we define. Based on this criterion, the two eigenstates in Fig. A2(d) are neither skin mode but normal bulk state distributions. Then, we calculate the spatial distribution of total eigenstates  $W(\mathbf{x})$  for such 1D ribbon, which is defined by the sum of all normalized right eigenstates in the ribbon for all  $k_x$ . The  $W(\mathbf{x})$  is almost uniform in the whole ribbon, indicating that there is no skin effect existence. Similarly, when the ribbon model is designed with OBCs along the

$y$  direction and PBCs in the  $x$  direction, as shown in Fig. A2(e), the corresponding projected bands are shown in Figs. A2(f) and (g). There is still no skin effect in this ribbon, as shown in Fig. A2(h).

Secondly, for the parallelogram-shaped ribbons, one of the structure is designed with OBCs along the  $k_2$  direction and PBCs along the  $y$  (or  $k_1$ ) direction, as shown in Fig. A3(a), where  $N_1 = 16$ . Although the structure is same as the structure in Fig. A2(a), the projected bands exhibit a different distribution due to different PBCs, as shown in Figs. A3(b) and (c). Interestingly, in this case, the eigenstates of projected bands at almost all k-points are localized at the top and bottom boundaries of the ribbon, manifesting a skin effect. The colorbar represents the degree of eigenstate localization at the boundary. We also select two k-points and plot their spatial distributions of eigenstates, which are indeed localized at the top and bottom boundaries of the ribbon, as shown in Fig. A3(d). Further, we calculate the spatial distribution of total eigenstates  $W(\mathbf{x})$ , indicating the skin effect. Furthermore, another structure is designed with OBCs along the  $k_1$  direction and PBCs along the  $k_2$  direction, as shown in Fig. A3(e), where  $N_2 = 16$ . We find that there is no skin effect in this case. Although the eigenstates at a few k-points are localized at the boundaries, the overall spatial distribution remains uniform, as shown in Figs. A3(f)-(h). In fact, in such a structure, we obtain

two vertical boundaries. Due to the trivial spectral winding number, it naturally does not exhibit a skin effect.

In summary, by opening boundaries along different directions, we observe the presence of boundary-dependent skin effects. Specifically, when boundaries along the horizontal and vertical directions are open, no skin effect emerges, as the spectral winding numbers in both directions are zero. However, when boundaries along the  $y = -x$  direction are open, a non-zero spectral winding number leads to the appearance of a skin effect at these boundaries [cf. Fig. 2].

### Appendix C: Volume law

In 2D systems exhibiting geometry-dependent skin effects, not all bulk states are skin modes. The number of skin modes satisfies the volume law, meaning that the number of skin modes scales proportionally with the volume of the system, i.e.

$$\delta N_s \propto \delta V, \quad (\text{C1})$$

where  $N_s$  represents the number of states which satisfies  $\eta'_b/\eta'_t > 80\%$ , and  $V = N_x \times N_y$  represents the volume (the total number of unit cells).

To verify the volume law, we calculate two shaped structures with different volume ( $V = 10 \times 10, 12 \times 12 \dots 20 \times 20$ ), and we discuss two case with  $\text{Im}(n) = 1$

and  $\text{Im}(n) = 0.1$ , respectively. We obtain the  $N_s$  under different geometry size, as shown in Fig. A4(c). Here, we also take a thickness of 2 unit cells as the boundary. The red and blue dashed line is the fitting curve for these data points with  $\text{Im}(n) = 1$  and  $\text{Im}(n) = 0.1$ , which shows that the  $N_s$  of parallelogram-shaped structure satisfies volume law while the square-shaped structure does not. For parallelogram-shaped structure, the relationships between  $N_s$  and  $V$  satisfy  $\delta N_s \approx 0.066\delta V$  ( $\delta N_s \approx 0.048\delta V$ ) for  $\text{Im}(n) = 1$  ( $\text{Im}(n) = 0.1$ ). For the square-shaped structure, it is evident that  $N_s$  and  $V$  do not satisfy a linear relationship. Therefore, we consider that the states corresponding to  $N_s$  in the square-shaped structure are not skin modes but rather localized states.

### ACKNOWLEDGMENTS

Z.-K. X., and Y. L. thank Liu Zheng-Rong, Chen Rui, and Lan Zhi-Hao for useful discussion. The work was supported by National Natural Science Foundation of China (Grants Nos. 11804087, 12074107, 62571212, 12374415, U25D8012), Natural Science Foundation of Hubei Province of China (Grants Nos. 2024AFA038, 2022CFB553, 2022CFA012, 2023AFB917), Wuhan City Key R&D Program (Grant No. 2025050602030069), and Program of Outstanding Young and Middle-aged Scientific and Technological Innovation Team of Colleges and Universities in Hubei Province of China (Grant No. T2020001).

- 
- [1] A. Bansil, H. Lin, and T. Das, Colloquium: Topological band theory, *Reviews of Modern Physics* **88**, 021004 (2016).
  - [2] M. Z. Hasan and C. L. Kane, Colloquium: topological insulators, *Reviews of Modern Physics* **82**, 3045 (2010).
  - [3] A. Burkov, Topological semimetals, *Nature materials* **15**, 1145 (2016).
  - [4] X.-L. Qi and S.-C. Zhang, Topological insulators and superconductors, *Reviews of Modern Physics* **83**, 1057 (2011).
  - [5] C.-K. Chiu, J. C. Teo, A. P. Schnyder, and S. Ryu, Classification of topological quantum matter with symmetries, *Reviews of Modern Physics* **88**, 035005 (2016).
  - [6] R. El-Ganainy, K. G. Makris, M. Khajavikhan, Z. H. Musslimani, S. Rotter, and D. N. Christodoulides, Non-hermitian physics and pt symmetry, *Nature Physics* **14**, 11 (2018).
  - [7] Z. Gong, Y. Ashida, K. Kawabata, K. Takasan, S. Higashikawa, and M. Ueda, Topological phases of non-hermitian systems, *Physical Review X* **8**, 031079 (2018).
  - [8] E. J. Bergholtz, J. C. Budich, and F. K. Kunst, Exceptional topology of non-hermitian systems, *Reviews of Modern Physics* **93**, 015005 (2021).
  - [9] M. Parto, Y. G. Liu, B. Bahari, M. Khajavikhan, and D. N. Christodoulides, Non-hermitian and topological photonics: optics at an exceptional point, *Nanophotonics* **10**, 403 (2020).
  - [10] B. Hu, Z. Zhang, H. Zhang, L. Zheng, W. Xiong, Z. Yue, X. Wang, J. Xu, Y. Cheng, X. Liu, *et al.*, Non-hermitian topological whispering gallery, *Nature* **597**, 655 (2021).
  - [11] H. Shen, B. Zhen, and L. Fu, Topological band theory for non-hermitian hamiltonians, *Physical review letters* **120**, 146402 (2018).
  - [12] M. A. Bandres, S. Wittek, G. Harari, M. Parto, J. Ren, M. Segev, D. N. Christodoulides, and M. Khajavikhan, Topological insulator laser: Experiments, *Science* **359**, eaar4005 (2018).
  - [13] Y. Zeng, U. Chattopadhyay, B. Zhu, B. Qiang, J. Li, Y. Jin, L. Li, A. G. Davies, E. H. Linfield, B. Zhang, *et al.*, Electrically pumped topological laser with valley edge modes, *Nature* **578**, 246 (2020).
  - [14] J. C. Budich and E. J. Bergholtz, Non-hermitian topological sensors, *Physical Review Letters* **125**, 180403 (2020).
  - [15] H.-K. Lau and A. A. Clerk, Fundamental limits and non-reciprocal approaches in non-hermitian quantum sensing, *Nature communications* **9**, 4320 (2018).
  - [16] H. Hodaei, A. U. Hassan, S. Wittek, H. Garcia-Gracia, R. El-Ganainy, D. N. Christodoulides, and M. Khajavikhan, Enhanced sensitivity at higher-order exceptional points, *Nature* **548**, 187 (2017).
  - [17] H. Wang, X. Zhang, J. Hua, D. Lei, M. Lu, and Y. Chen, Topological physics of non-hermitian optics and photonics: a review, *Journal of Optics* **23**, 123001 (2021).
  - [18] Q. Yan, B. Zhao, R. Zhou, R. Ma, Q. Lyu, S. Chu,

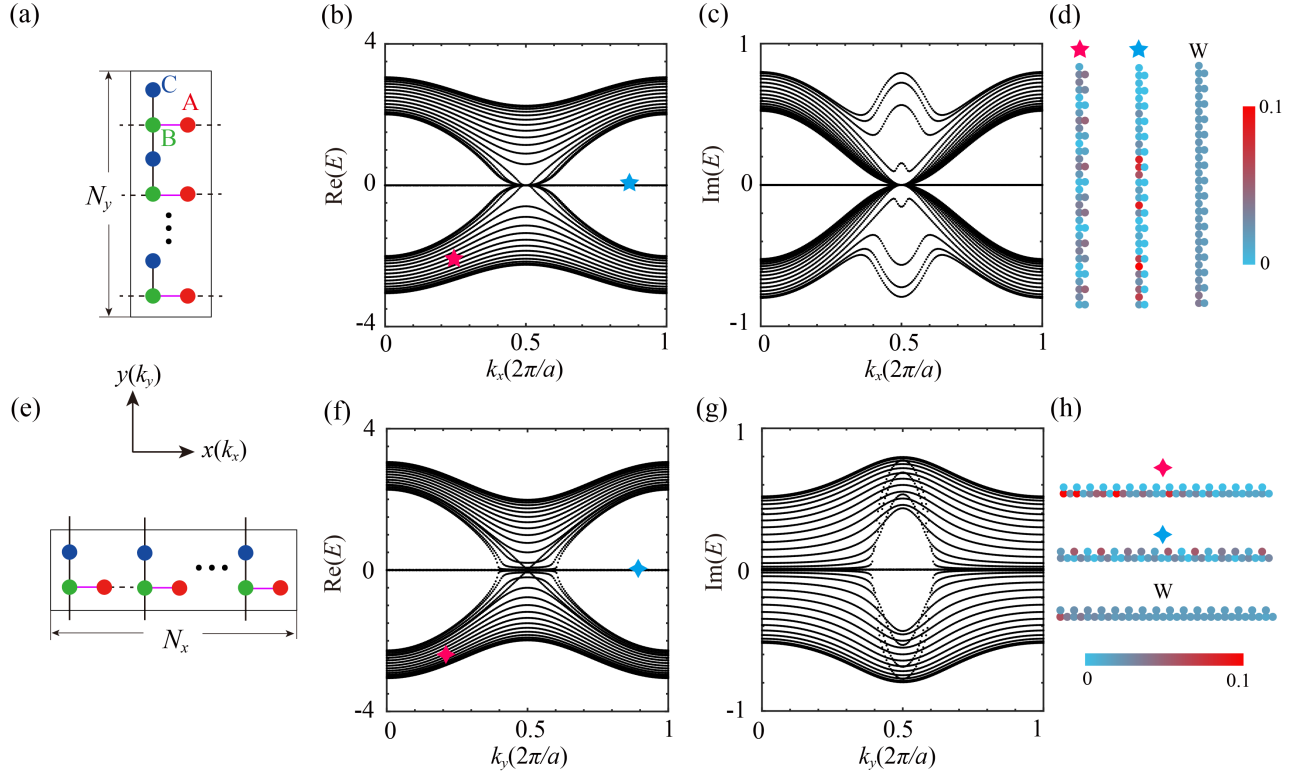


FIG. A2. (a) and (e) Super cell structures when we open vertical and horizontal boundaries. (b)-(c) and (f)-(g) The real and imaginary energy projected bands of two types of super cell. (d) and (h) The eigenstate distributions of marked and total eigenstates  $W(\mathbf{x})$  distributions of two ribbons.

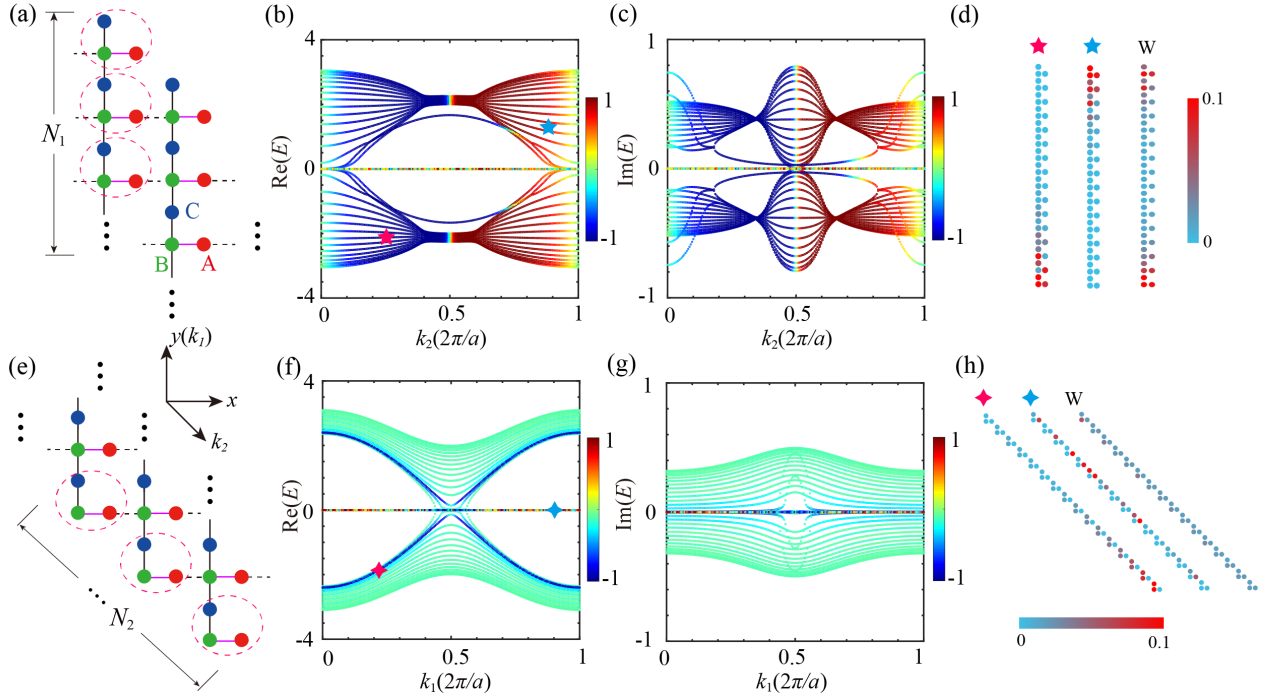


FIG. A3. (a) and (e) Super cell structures when we open  $k_1$  and  $k_2$  boundaries. (b)-(c) and (f)-(g) The real and imaginary energy projected bands of two types of super cell. (d) and (h) The eigenstate distributions of marked and total eigenstates  $W(\mathbf{x})$  distributions of two ribbons.

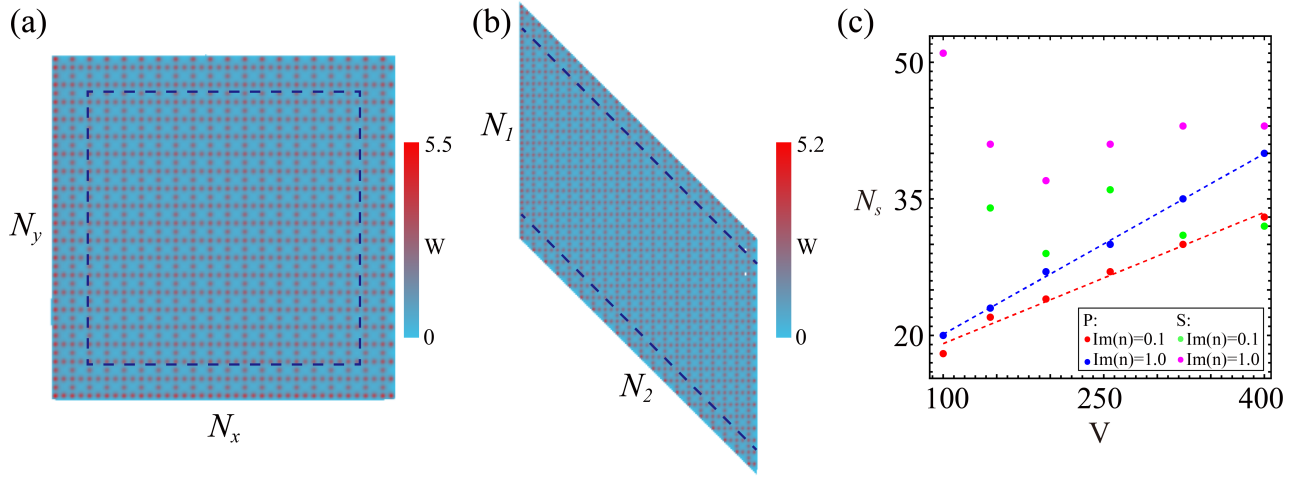


FIG. A4. (a)-(b) Spatial distribution of all eigenstates  $W(x)$  distributions of two shaped structures in Fig. 6. (c) The volume law in our system, the red and blue points is plotted by calculating data and the dashed line is the fitting curve showing  $\delta N_s \approx 0.066\delta V$  ( $\delta N_s \approx 0.048\delta V$ ) for  $\text{Im}(n) = 1$  ( $\text{Im}(n) = 0.1$ ).

- X. Hu, and Q. Gong, Advances and applications on non-hermitian topological photonics, *Nanophotonics* **12**, 2247 (2023).
- [19] H. Yuan, W. Zhang, Z. Zhou, W. Wang, N. Pan, Y. Feng, H. Sun, and X. Zhang, Non-hermitian topoelectrical circuit sensor with high sensitivity, *Advanced Science* **10**, 2301128 (2023).
- [20] K. Kawabata, K. Shiozaki, M. Ueda, and M. Sato, Symmetry and topology in non-hermitian physics, *Physical Review X* **9**, 041015 (2019).
- [21] S. Yao and Z. Wang, Edge states and topological invariants of non-hermitian systems, *Physical review letters* **121**, 086803 (2018).
- [22] D. S. Borgnia, A. J. Kruchkov, and R.-J. Slager, Non-hermitian boundary modes and topology, *Physical review letters* **124**, 056802 (2020).
- [23] N. Okuma, K. Kawabata, K. Shiozaki, and M. Sato, Topological origin of non-hermitian skin effects, *Physical review letters* **124**, 086801 (2020).
- [24] K. Zhang, Z. Yang, and C. Fang, Correspondence between winding numbers and skin modes in non-hermitian systems, *PHYSICAL REVIEW LETTERS Phys Rev Lett* **125**, 126402 (2020).
- [25] K. Kawabata, M. Sato, and K. Shiozaki, Higher-order non-hermitian skin effect, *Physical Review B* **102**, 205118 (2020).
- [26] X. Zhang, Y. Tian, J.-H. Jiang, M.-H. Lu, and Y.-F. Chen, Observation of higher-order non-hermitian skin effect, *Nature communications* **12**, 5377 (2021).
- [27] K. Zhang, Z. Yang, and C. Fang, Universal non-hermitian skin effect in two and higher dimensions, *Nature communications* **13**, 2496 (2022).
- [28] Q. Zhou, J. Wu, Z. Pu, J. Lu, X. Huang, W. Deng, M. Ke, and Z. Liu, Observation of geometry-dependent skin effect in non-hermitian phononic crystals with exceptional points, *Nature communications* **14**, 4569 (2023).
- [29] D. Guzmán-Silva, C. Mejía-Cortés, M. Bandres, M. Rechtsman, S. Weimann, S. Nolte, M. Segev, A. Szameit, and R. Vicencio, Experimental observation of bulk and edge transport in photonic lieb lattices, *New Journal of Physics* **16**, 063061 (2014).
- [30] S. Mukherjee, A. Spracklen, D. Choudhury, N. Goldman, P. Öhberg, E. Andersson, and R. R. Thomson, Observation of a localized flat-band state in a photonic lieb lattice, *Physical Review Letters* **114**, 245504 (2015).
- [31] F. Song, S. Yao, and Z. Wang, Non-hermitian topological invariants in real space, *Physical review letters* **123**, 246801 (2019).
- [32] S. Longhi, Probing non-hermitian skin effect and non-bloch phase transitions, *Physical Review Research* **1**, 023013 (2019).
- [33] J. Zhong, K. Wang, Y. Park, V. Asadchy, C. C. Wojcik, A. Dutt, and S. Fan, Nontrivial point-gap topology and non-hermitian skin effect in photonic crystals, *Physical Review B* **104**, 125416 (2021).
- [34] L. Zhang, Y. Yang, Y. Ge, Y.-J. Guan, Q. Chen, Q. Yan, F. Chen, R. Xi, Y. Li, D. Jia, *et al.*, Acoustic non-hermitian skin effect from twisted winding topology, *Nature communications* **12**, 6297 (2021).